



Conformable hierarchically engineered polymeric micromeshes enabling combinatorial therapies in brain tumours

Daniele Di Mascolo¹, Anna Lisa Palange¹, Rosita Primavera^{1,2}, Francesca Macchi¹, Tiziano Catelani^{1,3}, Federica Piccardi¹, Raffaele Spanò¹, Miguel Ferreira¹, Roberto Marotta⁴, Andrea Armirotti⁵, Alberto L. Gallotti⁶, Rossella Galli⁶, Christy Wilson⁷, Gerald A. Grant⁷ and Paolo Decuzzi¹✉

The poor transport of molecular and nanoscale agents through the blood-brain barrier together with tumour heterogeneity contribute to the dismal prognosis in patients with glioblastoma multiforme. Here, a biodegradable implant (μ MESH) is engineered in the form of a micrometre-sized poly(lactic-co-glycolic acid) mesh laid over a water-soluble poly(vinyl alcohol) layer. Upon poly(vinyl alcohol) dissolution, the flexible poly(lactic-co-glycolic acid) mesh conforms to the resected tumour cavity as docetaxel-loaded nanomedicines and diclofenac molecules are continuously and directly released into the adjacent tumour bed. In orthotopic brain cancer models, generated with a conventional, reference cell line and patient-derived cells, a single μ MESH application, carrying 0.75 mg kg^{-1} of docetaxel and diclofenac, abrogates disease recurrence up to eight months after tumour resection, with no appreciable adverse effects. Without tumour resection, the μ MESH increases the median overall survival ($\sim 30 \text{ d}$) as compared with the one-time intracranial deposition of docetaxel-loaded nanomedicines (15 d) or 10 cycles of systemically administered temozolomide (12 d). The μ MESH modular structure, for the independent coloaded of different molecules and nanomedicines, together with its mechanical flexibility, can be exploited to treat a variety of cancers, realizing patient-specific dosing and interventions.

High-grade malignant gliomas are characterized by a poor prognosis with a median overall survival (OS) lower than two years and a five-year survival rate below 10% (refs. 1–5). Even more remarkable is the fact that glioblastoma multiforme (GBM) prognosis and treatment strategy have not changed over the past 20 years: surgical resection of the primary mass followed by adjuvant radiation and systemic chemotherapy with temozolomide (TMZ) continue to be the sole approach^{6,7}. GBM has the tendency to infiltrate the normal brain tissue^{8,9}, thus causing disease recurrence already by six months after resection, usually adjacent to the original resection cavity^{10,11}. Additional factors contributing to the poor GBM prognosis are related to its heterogeneity and the presence of the blood–brain barrier (BBB), which limits drug penetration^{12–15}.

While systematic interpatient genetic analyses identified different GBM transcriptional subgroups^{16–19}, patient-specific analyses documented the heterogeneous nature of the malignant tissue, where different cancer stem cells coexist with one another^{20,21}. As such, high-grade gliomas would contain subsets of cells with different sensitivities to therapeutic molecules²², suggesting that combination therapies could improve prognosis over monotherapies, especially after resection^{23–26}. Furthermore, most systemically administered therapeutic agents, at both the nano- and molecular scales, generally achieve moderate to negligible brain accumulation levels, because of the BBB^{15,27,28}. Different strategies continue to be tested to reversibly open this biological barrier, including the administration of vascular permeation enhancers^{29,30}, and the

application of focused ultrasound^{31–33}. Also, specific ligand molecules targeting the malignant microvasculature have been identified to support transcytosis across the BBB^{34,35}. So far, some of these approaches have succeeded in increasing the perivascular localization of bloodborne therapeutic agents across the BBB but not their deep permeation into the brain tissue.

Locoregional therapies via drug depots directly inserted at the edge of the tumour resection cavity and convection-enhanced drug delivery appear as appealing alternatives to systemic administration^{36,37}, particularly in the case of brain tumours, as these would circumvent the BBB and deliver sizable numbers of drug molecules to the tumour bed. In the late 1990s, a biodegradable wafer encapsulating carmustine was introduced for GBM treatment³⁸. Despite a two-month improvement in median survival time, this implant has been seldom used³⁹. Recently, the same wafer was upgraded to co-release carmustine and TMZ, confirming preclinically a clear advantage for the combination therapy⁴⁰. While the convection-enhanced infusion of small molecules and nanoparticles in the tumour mass has often led to contradictory results^{37,41,42}, polymeric in situ forming implants, patches and fibres continue to be actively explored for the sustained release of a variety of chemotherapeutic^{43–48} and immunotherapeutic molecules^{49,50}. Layered, flexible patches integrating microelectrodes have also been proposed for the remotely controlled release of anticancer drugs in the brain⁵¹. The relevance of locoregional administration is further emphasized by recent results obtained on chimaeric antigen

¹Laboratory of Nanotechnology for Precision Medicine, Fondazione Istituto Italiano di Tecnologia, Genoa, Italy. ²Interventional Regenerative Medicine and Imaging Laboratory, Department of Radiology, Stanford University, Palo Alto, CA, USA. ³Microscopy Facility, University of Milano-Bicocca, Milan, Italy.

⁴Electron Microscopy Facility, Fondazione Istituto Italiano di Tecnologia, Genoa, Italy. ⁵Analytical Chemistry Lab, Fondazione Istituto Italiano di Tecnologia, Genoa, Italy. ⁶Neural Stem Cell Biology Unit, Division of Neuroscience, San Raffaele Scientific Institute, Milan, Italy. ⁷Department of Neurosurgery, Stanford University, Palo Alto, CA, USA. ✉e-mail: paolo.decuzzi@iit.it

receptor T cell (CAR-T cell)-based immunotherapies in the treatment of brain tumours^{52,53}. Yet, the therapeutic efficacy of intracranial drug depots continues to be impaired by the limited drug penetration and distribution within the diseased tissue.

In this study, the fabrication, characterization and preclinical testing of a polymeric micromesh (μ MESH) is reported for the combinatorial treatment of GBM. The μ MESH comprises two different compartments: a micrometric poly(lactic-co-glycolic acid) (PLGA) mesh (compartment 1), carrying hydrophobic small molecules, deposited over a poly(vinyl alcohol) (PVA) layer (compartment 2), embedding nanomedicines. Upon dissolution of the PVA layer, nanomedicines are released and the PLGA mesh establishes an intimate interaction with the surrounding biological environment. This boosts the μ MESH therapeutic efficacy as compared with multiple control (CTRL) groups in three different orthotopic brain tumour models over an eight-month observation period.

Results

Fabrication and hierarchical structure of the μ MESH. A top-down fabrication approach is employed to realize the μ MESH, whereby specific geometrical features are transferred from a silicon master template to a PVA layer, passing through an intermediate polydimethylsiloxane (PDMS) template (Fig. 1a). Both the original silicon template and the final PVA layer feature a regular array of $20 \times 20 \mu\text{m}^2$ micropillars with a $3 \mu\text{m}$ pitch. This geometric arrangement is documented by the electron microscopy images shown in Fig. 1b for the silicon (top) and PDMS (bottom) templates. Over the final PVA layer, a polymeric PLGA paste is uniformly dispersed to accurately fill up the empty ridges within the micropillars. Upon solvent evaporation, a solid PLGA mesh is returned, comprising a regular network of polymeric strands with a $3 \times 5 \mu\text{m}^2$ rectangular cross-section defining arrays of $20 \mu\text{m}$ square holes (Fig. 1c). The strands and holes of this PLGA mesh reproduce the geometry of the PDMS template (Fig. 1b, bottom). Furthermore, during the μ MESH realization, hydrophilic molecules and nanoparticles can be readily dispersed within the PVA layer too. For instance, 200 nm spherical polymeric nanoparticles (SPNs), labelled with the red fluorescent molecule rhodamine B (RhB), are incorporated in the PVA layer (Fig. 1d).

As such, the μ MESH appears as a dual-compartment, hierarchically engineered drug depot where hydrophobic agents are dispersed within the PLGA strands while hydrophilic agents are incorporated in the PVA layer (Fig. 1e (left)). The fluorescent microscopy image in Fig. 1e (centre) presents a continuous green signal, associated with curcumin (CURC)-loaded PLGA strands, and a punctuated red signal, related to the RhB-SPNs dispersed in PVA. Figure 1e (right) shows the PLGA mesh and a plethora of SPNs, embedded within a partially dissolved PVA layer. These images document the regular structure of the polymeric mesh as well as the uniform distribution of its payloads within the two separate compartments. Given the top-down fabrication approach, the μ MESH geometry can be precisely tuned in size and shape.

In vitro functional characterization of the μ MESH. In a physiological solution, the PVA layer progressively dissolves and releases its cargo. This is demonstrated in Fig. 2a, where a CURC-loaded mesh deposited over a PVA layer incorporating RhB-SPNs is exposed to an aqueous solution. Due to the overlap of CURC (green) and RhB-SPN (red) fluorescence, the μ MESH appears initially yellowish. However, as time progresses, more RhB-SPNs are released, turning the solution red and the polymeric mesh green (Fig. 2a and Supplementary Fig. 1). This documents the dual-compartment feature of the μ MESH.

A similar experiment was also conducted with free RhB molecules, substituting for RhB-SPNs (Supplementary Fig. 2). In Fig. 2b, the fluorescent intensity of the solution is plotted against the

separation distance from the μ MESH edge (black dashed line, Fig. 2a) for free RhB and RhB-SPNs, at 0 and 5 min. As expected, the nanoparticles (red curve) diffuse more slowly in the surrounding solution than RhB (blue curve). Importantly, the SPNs released from the PVA layer (μ SPNs) preserve their spherical shape and narrow size distribution but tend to be slightly different from the original SPNs in terms of size and surface electrostatic potential ζ (Fig. 2c). While the original SPNs (before entrapment in PVA) have an average hydrodynamic diameter of $189.3 \pm 1.1 \text{ nm}$ and a ζ of $-50.0 \pm 1.7 \text{ mV}$, the μ SPNs (released from PVA) present an average size of $236.3 \pm 0.4 \text{ nm}$ and a ζ of $-33.2 \pm 1.0 \text{ mV}$. This change could be ascribed to the formation of a nanoscopic PVA coating over the SPNs, which tends to dissolve slowly over time. Indeed, after 15 d of incubation in a physiological solution, the μ SPN size reduces asymptotically to $\sim 190 \text{ nm}$ (Supplementary Fig. 3). The presence of a PVA coating was also confirmed via a cryo-TEM (transmission electron microscopy) analysis (Supplementary Fig. 4a,b), returning particle diameters comparable to those quantified above via dynamic light scattering measurements, and a liquid chromatography–mass spectrometry analysis (Supplementary Fig. 4c,d), detecting PVA only on μ SPNs. This residual PVA layer could persist for over 15 d, in agreement with previous reports^{54,55}.

As the PVA dissolves, the μ MESH network of flexible $3 \times 5 \mu\text{m}^2$ PLGA strands emerges (Fig. 2d) and could conform around complex surfaces. This can be appreciated in Fig. 2e, where the μ MESH wraps around a GBM tumour spheroid. The projected side views clearly demonstrate the intimate interaction between the tumour spheroid (green) and the μ MESH (red). Notice that such wrapping cannot be realized with a flat PLGA substrate (FLAT) (Supplementary Figs. 5 and 6).

A wrapping μ MESH could more effectively release its chemotherapeutic cargo directly in the malignant mass, as opposed to a flat, non-conforming PLGA layer. To confirm this, the μ MESH and FLAT were loaded with the same amounts of docetaxel (DTXL), a potent chemotherapeutic molecule. The pharmacological properties of FLAT were finely tuned to ensure the same DTXL release rates as for the μ MESH (Supplementary Fig. 7a,b). For a DTXL dose of 100 nM, the μ MESH inhibits tumour spheroid growth more efficiently than FLAT, leading to a zero proliferation rate (Fig. 2f). In contrast, the diameter of spheroids treated with FLAT almost triples in 15 d.

In vitro pharmacological activity of the μ MESH. To include anticancer therapeutic properties, the μ MESH was loaded with DTXL-SPNs, integrated in the PVA layer, and diclofenac (DICL) molecules, dispersed within the PLGA strands. On the basis of a previous work by the authors, DTXL-SPNs are expected to act directly on the malignant cells while DICL would sensitize them to chemotherapy²³. Given the μ MESH structure, several other therapeutic agents and combinations thereof could be readily included.

DTXL-SPNs present similar physicochemical properties to other SPN configurations and an encapsulation efficiency of $23.31 \pm 4.97\%$ ($466.3 \pm 99.4 \mu\text{g}$ of DTXL per preparation) (Supplementary Figs. 8 and 9a). DTXL can be dosed by changing the initial number of DTXL-SPNs, returning a linear loading curve with a constant embedding efficiency of $\sim 50\%$ (Fig. 3a and Supplementary Fig. 9c–e). DTXL is slowly released from the SPNs within $\sim 3 \text{ d}$ following a classical, diffusion-driven profile (Fig. 3b and Supplementary Fig. 9b).

As for DICL, the total embedded drug mass also increases in a linear fashion with the feeding amount (Fig. 3c). The embedding efficiency for DICL ranges between 45% and 60%, depending on the input (Supplementary Fig. 10). After an initial burst, DICL is slowly released at pharmacologically relevant doses for about a month, with a released amount of $0.15 \mu\text{g}$ at two weeks (Fig. 3d). Given the accurate control in DTXL and DICL loading, their ratio can be

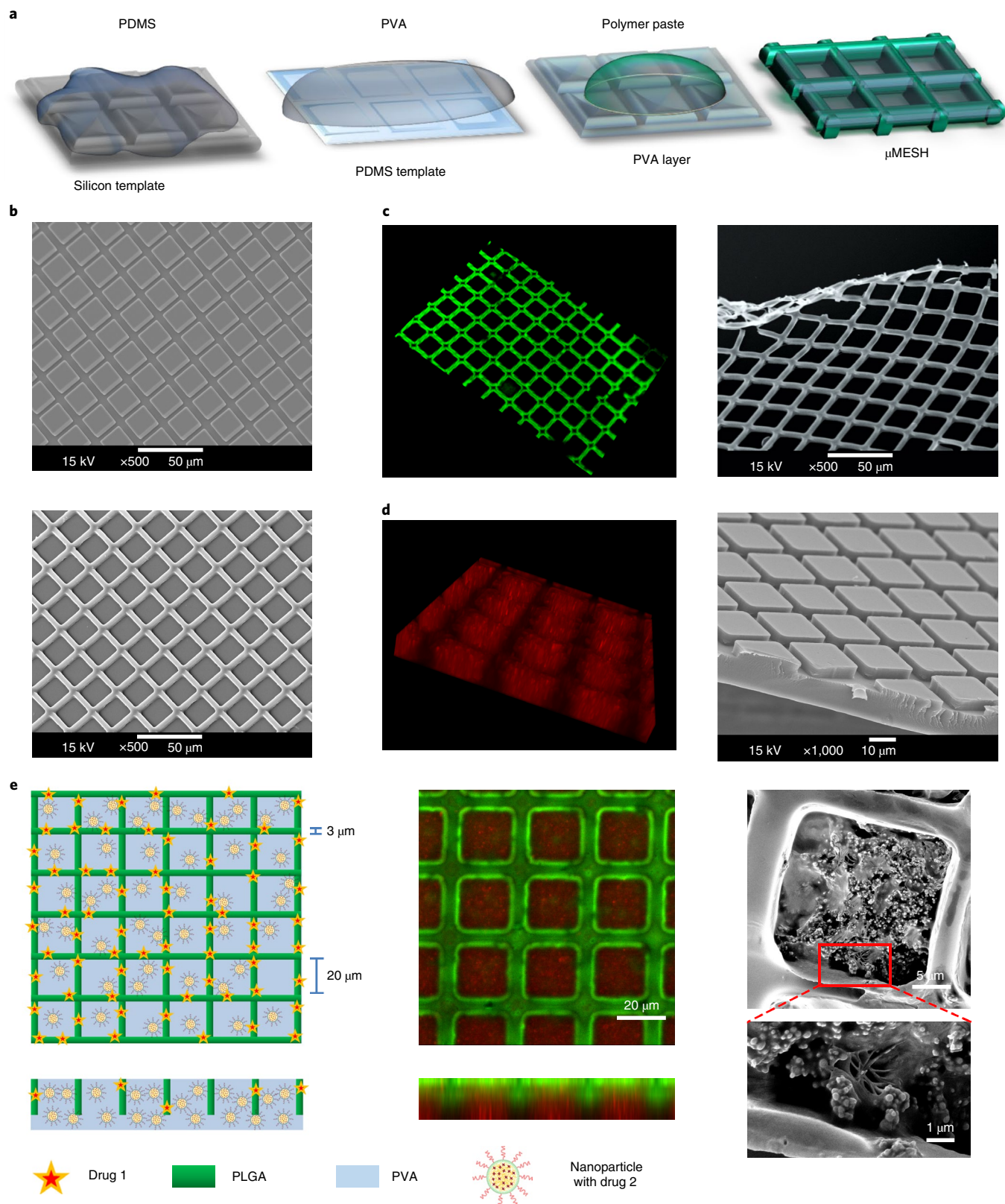


Fig. 1 | Fabrication and hierarchical structure of the μ MESH. **a**, Multistep procedures for μ MESH realization. **b**, Scanning electron microscope (SEM) images of the master silicon template (top) and intermediate PDMS template (bottom), demonstrating the accuracy of the replica process. **c**, Confocal microscopy and SEM images of the PLGA mesh loaded with CURC (green) following full dissolution of the PVA layer. **d**, Confocal microscopy and SEM images of the PVA layer entrapping RhB nanoparticles (red). The $20 \times 20 \mu\text{m}^2$ pillars in the PVA template appear brighter than the surrounding ridges because of their higher volume and, consequently, higher local number of RhB nanoparticles. **e**, Schematic representation of the $5 \times 5 \text{mm}^2$ μ MESH structure (left), highlighting the $3 \times 5 \mu\text{m}^2$ PLGA strands loaded with drug 1 and the PVA layer loaded with nanomedicines (drug 2). The schematic matches the confocal microscopy image (centre) showing the CURC-loaded PLGA strands (green) and the PVA layer carrying RhB nanoparticles (red), as well as the SEM images (right) displaying individual SPNs in the PVA layer.

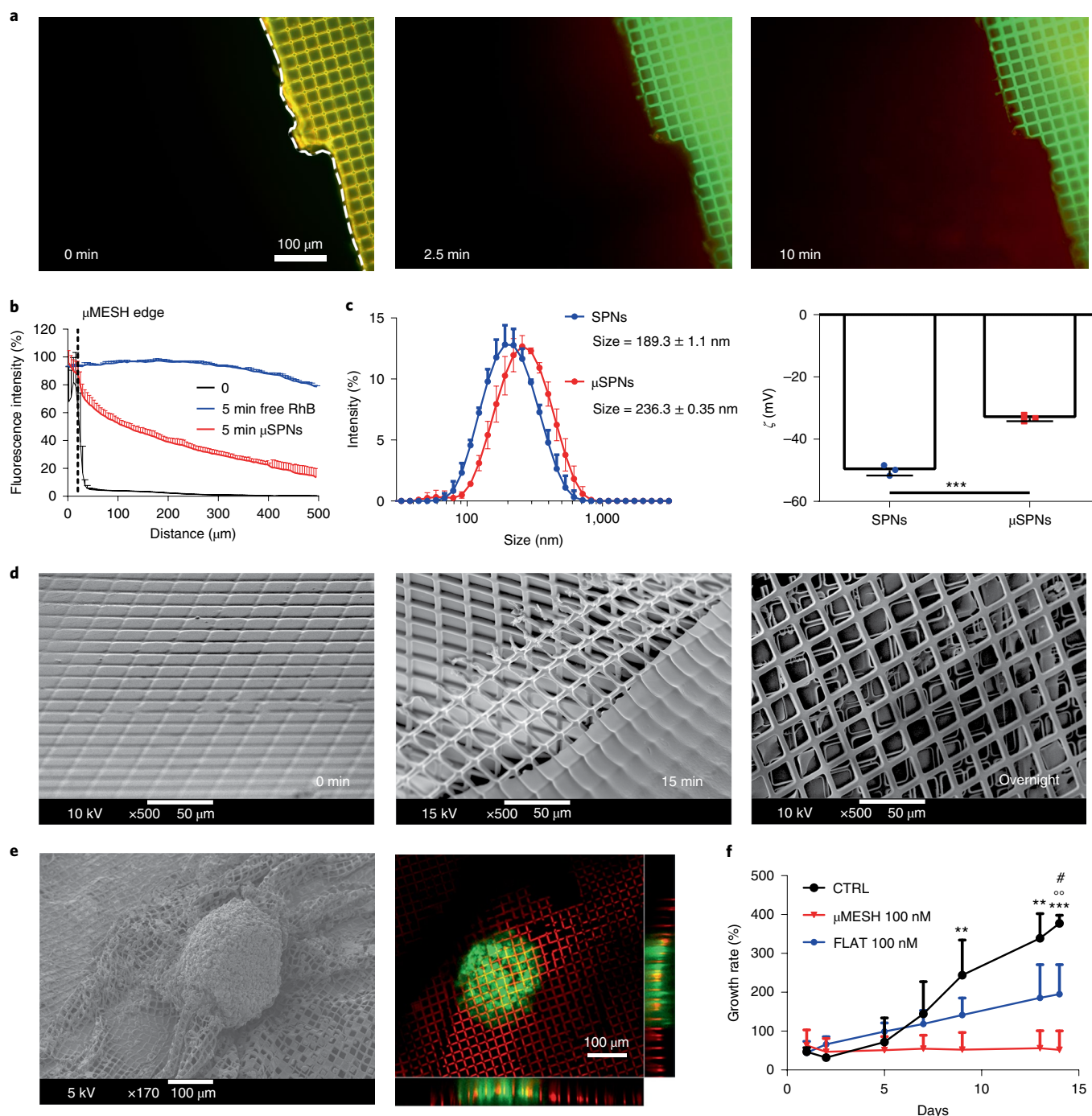


Fig. 2 | In vitro functional characterization of the μMESH . **a**, Release of RhB nanoparticles from the μMESH , following the PVA layer dissolution at different time points. The red signal of the diffusing RhB nanoparticles rapidly grows in solution as the CURC-loaded μMESH turns from yellow to green. **b**, Variation of the fluorescence intensity for free RhB molecules (blue line) and RhB nanoparticles (red line) in solution against the distance from the μMESH edge (black dashed line). (Data are expressed as mean \pm s.d.) **c**, Hydrodynamic diameter and ζ of SPNs before entrapment into PVA (SPNs) and after release from PVA (μSPNs). The latter are larger and less negatively charged as compared with the original SPNs. (Data are expressed as mean \pm s.d., $n=3$ independent samples.) Statistical significance was determined by two-tailed *t*-test. $***P=0.00011$. **d**, SEM images of the μMESH showing the emerging network of PLGA strands following PVA dissolution after incubation in aqueous solution. **e**, SEM and confocal microscopy images showing the μMESH (red) wrapping around a GFP⁺ U-87 MG GBM spheroid (green). **f**, Growth rates for a U-87 MG spheroid treated with a 100 nM DTXL-loaded μMESH (red line), a 100 nM DTXL-loaded FLAT substrate (blue line) and the untreated case (CTRL—black line). (Data are expressed as mean \pm s.d., $n=4$ independent spheroids. The statistically significant difference was evaluated by one-way analysis of variance: day 9, $P=0.0068$; day 13, $P=0.0081$; day 14, $P=0.0006$. Post hoc Tukey multiple comparison test results were the following: day 9, $**P=0.005$ for μMESH versus CTRL; day 13, $**P=0.008$ for μMESH versus CTRL; day 14, $\#P=0.045$ for μMESH versus FLAT; $^{\circ}P=0.0054$ for FLAT versus CTRL; $***P=0.0006$ for μMESH versus CTRL).

modified a priori during the μ MESH fabrication within an ample range of concentrations by readily changing the input amounts of DTXL-SPNs and DICL.

Then, the in vitro therapeutic efficacy of the μ MESH was tested on U-87 MG green fluorescent protein (GFP)⁺ spheroids in addition to conventional experiments on cell monolayers (Supplementary Figs. 11 and 12). Six experimental groups were considered, including free DICL, free DTXL, the combination of free DTXL and DICL (DTXL/DICL), μ SPNs, the μ MESH loaded with DICL and DTXL-SPNs and the empty μ MESH. The size of the tumour spheroid was monitored for 8 d (Fig. 3e and Supplementary Figs. 13 and 14) and a half-maximum inhibitory concentration (IC₅₀) value was estimated by measuring the red fluorescence intensity (cell death) associated with each spheroid (Fig. 3f). The μ MESH was more effective than all other treatments already in vitro, returning an IC₅₀ of \sim 1.6 nM. The same trend was observed when assessing the tumour spheroid size over time (Fig. 3g and Supplementary Figs. 15 and 16). The ability of the μ MESH to outperform all other treatment strategies is even clearer when analysing the tumour spheroid growth rates on days 1 and 8 after treatment (Fig. 3h). A statistically significant difference between μ SPNs and μ MESH can be appreciated already at 1 nM. Also, the μ MESH only induced a negative growth rate on day 8. This demonstrates the higher pharmacological activity of the μ MESH as compared with other therapeutic groups, including the direct μ SPN application and FLAT (Supplementary Figs. 5, 6 and 16).

Tissue transport performance of μ MESH-released nanoparticles.

As mentioned above, μ SPNs have a slightly larger diameter and surface electrostatic potential than SPNs, which could affect their tissue penetration. The transport of μ SPNs and SPNs was tested side by side in five different assays.

In a first experiment, the penetration depth of RhB-labelled nanoparticles was assessed in a Matrigel matrix, mimicking the tumour microenvironment⁵⁶ (Fig. 4a–c). Equal numbers of μ SPNs and SPNs (Supplementary Fig. 17) were deposited above the Matrigel and observed to slowly permeate into the gel (Fig. 4b). By analysing similar images, the fluorescence profile was generated at different time points. While at 4 h the fluorescence profiles of the two nanoparticles are relatively similar, significant statistical differences start to appear in the 0–500 μ m region already at 12 h and in deeper regions at 36 h (Fig. 4c and Supplementary Figs. 18 and 19).

In a second assay, SPNs loaded with 10 nm gold nanoparticles (AuNPs) and tagged with Cy5 molecules (Au-Cy5-SPNs) were incubated with U-87 MG spheroids to perform correlative light-electron microscopy (CLEM) imaging. The size and surface properties of Au-Cy5-SPNs were comparable to those of the other SPN configuration (Supplementary Fig. 20). After incubation with equal numbers of nanoparticles, tumour spheroids were cut into multiple slices, then the relative mean fluorescence was measured on different concentric annuli and normalized to the mean fluorescence of the whole spheroid area (Fig. 4d and Supplementary Fig. 21). The two types of nanoparticle exhibited different distribution

patterns, with SPNs forming isolated clusters on the spheroid and μ SPNs presenting a more uniform distribution around and inside the spheroid (Fig. 4e). The fluorescence intensity decreases from the spheroid surface (-200μ m) to the core (0), with SPNs showing the strongest reduction (Fig. 4f and Supplementary Fig. 23). This trend was also confirmed by analysing the same slices via TEM for AuNPs (Supplementary Fig. 22).

In the third experiment, Cy5-labelled nanoparticles were deposited on the surface of the brain in healthy mice. After 3 d, the fluorescent signal was acquired via spinning-disc confocal microscopy, returning an almost twofold statistically significant increase in μ SPN accumulation (Supplementary Figs. 24 and 25).

In the fourth assay, the whole μ MESH was deposited on the brain surface of healthy mice and intravital microscopy was used to measure the penetration depth of Cy5-labelled nanoparticles. As μ SPNs were continuously released from the μ MESH, the intensity fluorescent profile was detected over 10 d as a function of the penetration depth (Fig. 4g). This plot shows an increase over time of the nanoparticle concentration in deep brain regions underneath the μ MESH. Notably, a still relevant concentration gradient is observed at day 10, which would suggest that particle penetration may continue for longer times after the μ MESH application (Supplementary Fig. 26).

In the fifth assay, SPNs and the μ MESH were deposited on the surface of a malignant mass. Again, μ SPNs appeared to be retained more efficiently within the area of the μ MESH application (Fig. 4h) and penetrate deeper within the tumour tissue as compared with SPNs (Fig. 4i and Supplementary Fig. 27).

All these in vitro and in vivo characterizations confirm that μ SPNs released from a conforming μ MESH can permeate biological tissues more efficiently than SPNs. This behaviour could be ascribed to the lower negative ζ , which has been shown to mitigate the adhesive interactions with the extracellular matrix^{57,58}; the nanoscopic PVA coating, which could facilitate particle sliding as it progressively dissolves⁵⁹; and the μ MESH intimate contact with the surrounding environment, which would realize a depot at the tumour margins with a very highly localized nanoparticle gradient.

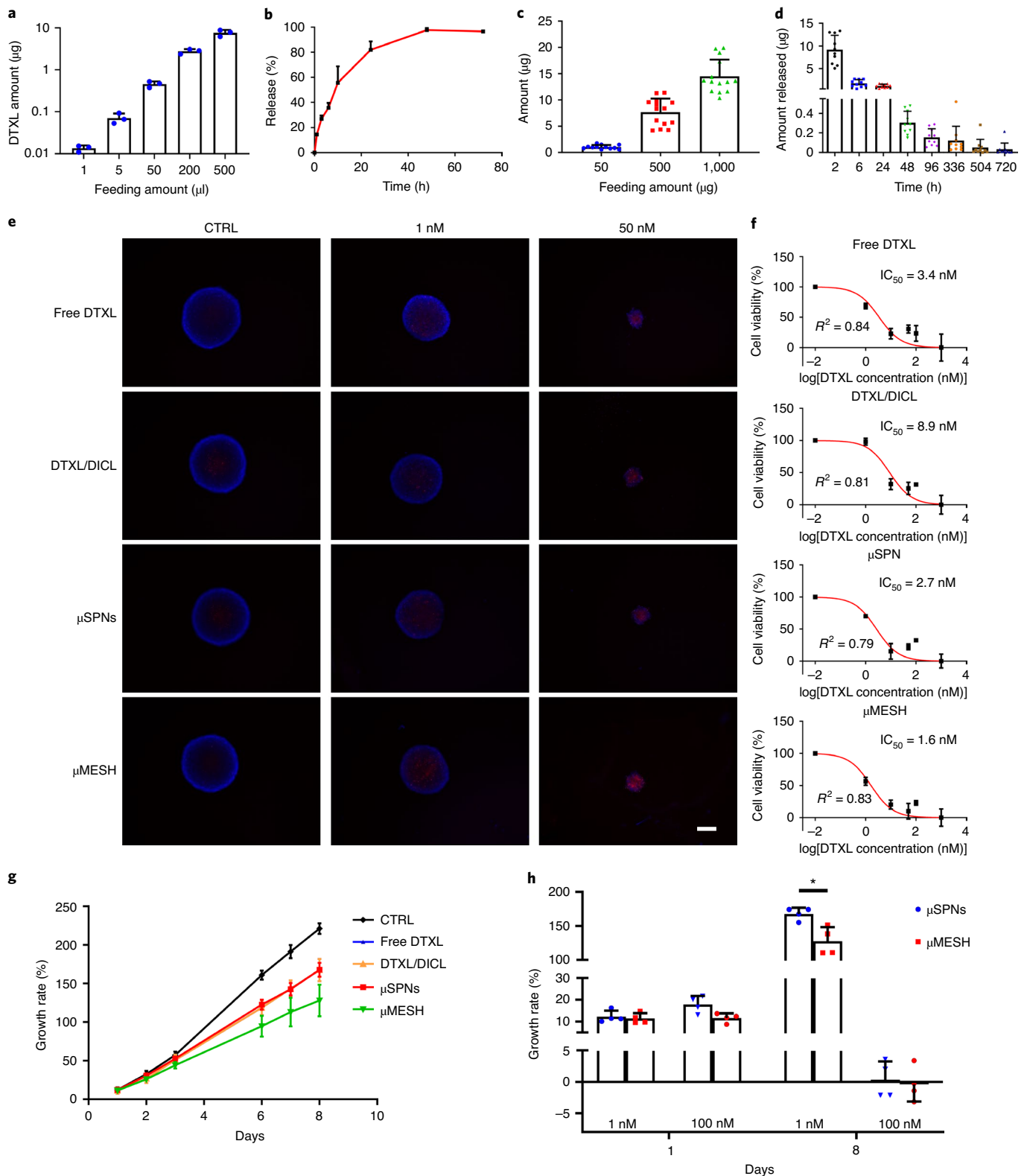
Preclinical therapeutic efficacy of the μ MESH. Murine orthotopic models of glioblastoma were used to test in vivo the therapeutic potential of the μ MESH as compared with the clinical standard TMZ and other CTRL groups. Two different cell types were used: the glioma cell line U-87 MG Luc⁺, which still represents a standard reference in the field; and patient-derived Luc⁺ cancer stem cells (hCSCs)⁶⁰. These cells were injected into the prefrontal cortex 1.0 mm from the skull in the ‘no tumour removal’ model and 0.75 mm from the skull in the ‘tumour removal’ model (Fig. 5a,b). Treatments were initiated only after detecting a strong bioluminescence signal (1×10^6 p s⁻¹ cm⁻² sr⁻¹—Supplementary Fig. 28), confirming a stable tumour growth.

In the no tumour removal model, the therapeutic efficacy of the μ MESH was tested against eight different CTRL groups, including three systemic treatments—intravenously injected (i.v.) TMZ, i.v. DTXL and SPNs loaded with DTXL and DICL (i.v. SPNs); four

Fig. 3 | In vitro pharmacological activity of the μ MESH. **a**, DTXL amount in the μ MESH growing quasilinearly with the initial input of DTXL-SPNs dispersed in the PVA layer ($n=3$ independent samples). **b**, Release profile over time for DTXL from DTXL-SPNs ($n=3$ independent samples). **c**, DICL amount in the μ MESH growing quasilinearly with the initial input of DICL dispersed within the PLGA mesh ($n=12$ independent samples per 50 μ g and 14 independent samples for 500 and 1,000 μ g). **d**, Release profile over time for DICL from the μ MESH. Data are presented as instantaneous rates rather than cumulative drug release rates. Note that, in confined volumes, these DICL doses are clinically relevant ($n=10$ independent samples). **e**, Representative fluorescent images of U-87 MG GFP⁺ spheroids (green channel not shown here) after 8 d of treatment with free DTXL, free DTXL/DICL, μ SPNs and μ MESH at two different drug concentrations, namely 1 and 50 nM (blue, nuclei; red, propidium iodide staining for dead cells) (scale bar: 250 μ m). **f**, IC₅₀ curves for the U-87 MG GFP⁺ spheroids subjected to the above-listed treatments. (Data are expressed as mean \pm s.e.m., $n=4$ independent samples.) **g**, Growth rate of U-87 MG GFP⁺ spheroids subjected to the above-listed treatments, at 1 nM equivalent DTXL ($n=4$ independent samples). **h**, Comparison between growth rates, on days 1 and 8, of U-87 MG GFP⁺ spheroids treated with SPNs and μ MESH, for 1 and 100 nM equivalent DTXL. ($*P=0.0119$, for the comparison of the same concentration, on the same day, in the two groups, by the two-tailed *t*-test.) (Data are expressed as mean \pm s.d., $n=4$ independent samples).

local treatments—empty μ MESH, μ MESH loaded with DICL only (DICL- μ MESH), μ MESH loaded with DTXL only (DTXL- μ MESH) and locally deposited SPNs (L-SPNs); and the untreated mouse (CTRL). Note that both SPNs and L-SPNs are loaded with DTXL and DICL in the same ratio as the μ MESH (Supplementary Fig. 29). In the no tumour removal model, a drop in radiance is documented

for the μ MESH as compared with all other groups (Fig. 5c and Supplementary Figs. 30–32). Equally informative are the Kaplan–Meyer curves in Fig. 5c, where all the mice eventually succumb except for one mouse in the μ MESH group that survives until day 250. The μ MESH extended the OS by almost threefold as compared with TMZ, and by twofold against the local and systemic SPN treat-



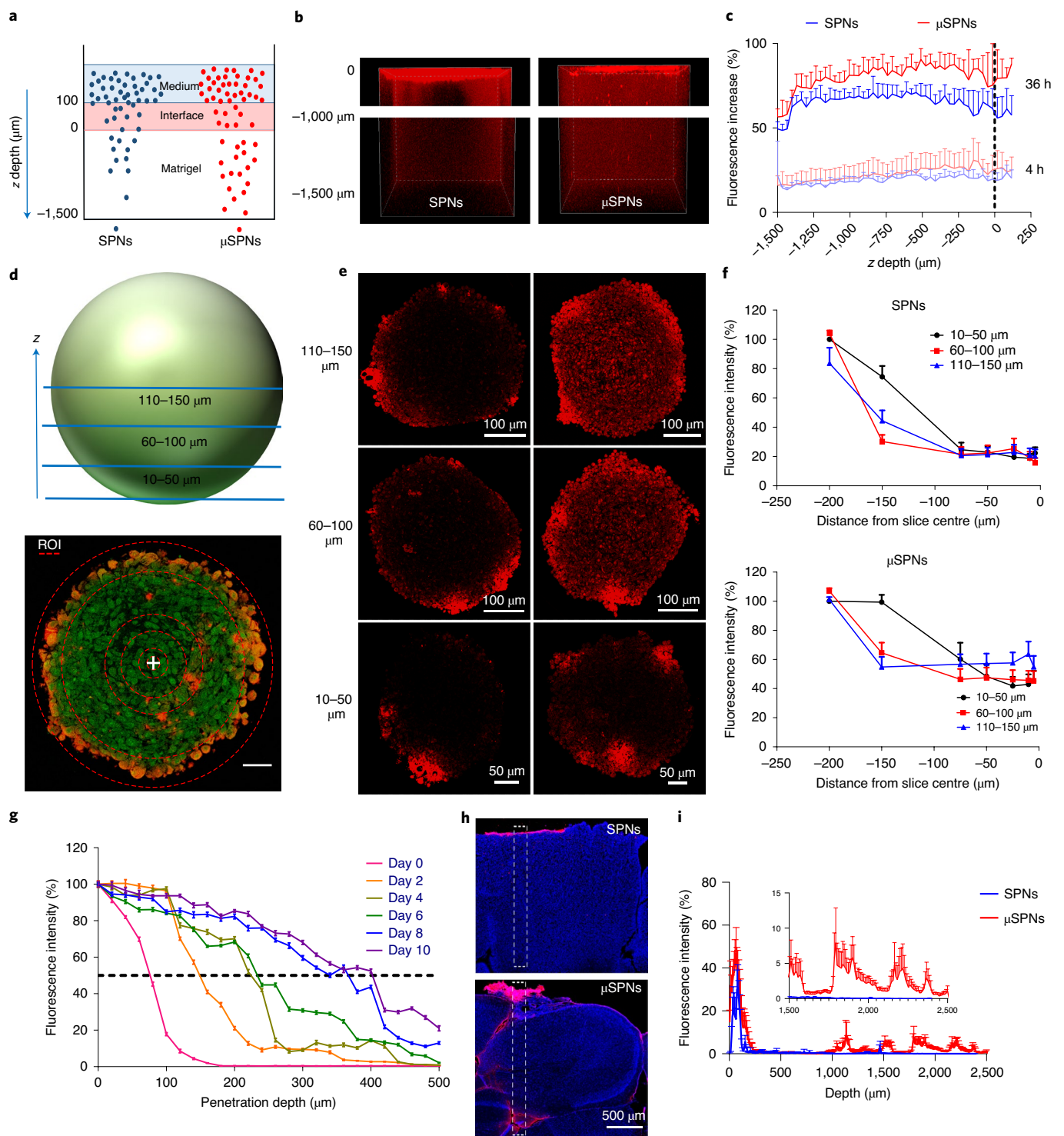
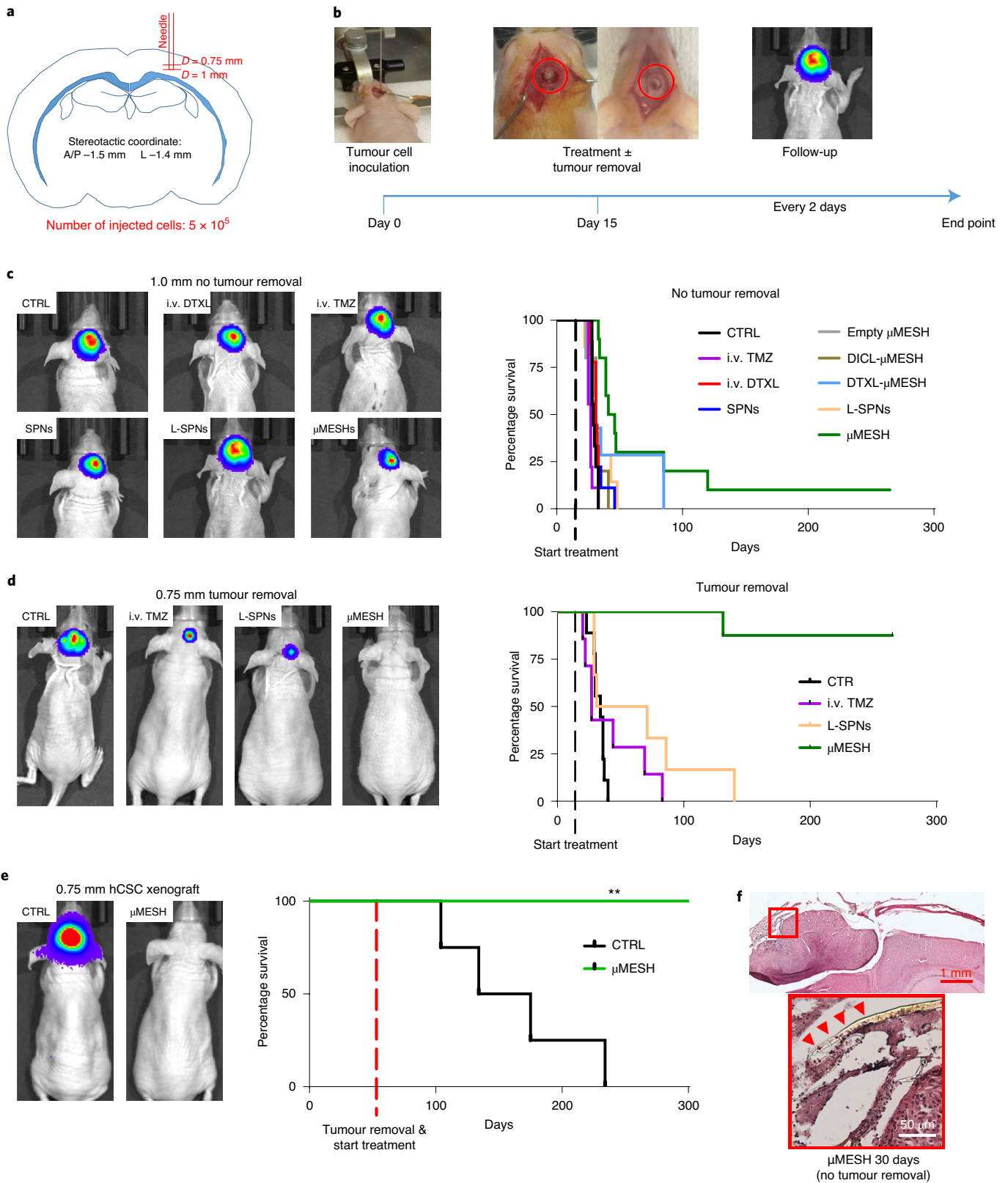


Fig. 4 | Tissue transport performance of μ MESH-released nanoparticles. **a**, Schematic representation of a square well in a microscope slide filled with Matrigel and medium. **b**, Representative confocal three-dimensional reconstruction images of Matrigel enriched with slowly diffusing nanoparticles, at 36 h. **c**, Percentage increase in fluorescence intensity in Matrigel along the z axis, orthogonal to the well bottom. (Data are expressed as mean \pm s.d., $n=6$ independent samples.) **d**, Schematic representation of a U-87 MG GFP⁺ spheroid (top) identifying the location of the slices used in the penetration studies, and optical fluorescent image (bottom) of a representative slice showing the concentric annuli used for analysis (scale bar: 50 μ m). **e**, Representative fluorescent images of slices cut at different heights in the spheroid, where the red signal is associated with Cy5-labelled nanoparticles. **f**, Mean fluorescence intensity on the slice regions plotted along the radius of the spheroid, from the surface (-200μ m) to the core (0μ m). (Data are expressed as mean \pm s.e.m., $n=15$ slices for each of the three regions over three independent samples.) **g**, Fluorescent intensity profile along the direction normal to the brain surface for Cy5-labelled μ SPNs, released from μ MESH deposited in healthy mice. (Data are expressed as mean \pm s.d., $n=9$ regions of interest (ROIs) for each of the three animals.) **h**, Spatial distribution of SPNs and μ SPNs 8 d after deposition over the brain of tumour-bearing mice. The dashed rectangle represents one of 12 different adjacent ROIs considered for the analysis, per slide. **i**, Averaged fluorescence intensity profile along the direction normal to the brain surface (that is, depth = 0) to the inner part of the brain (depth = $2,500 \mu$ m) for SPNs and μ SPNs. (Data are expressed as mean \pm s.e.m., $n=12$ adjacent ROIs for each of the three independent samples.)



ments and the DTXL-μMESH. These *in vivo* results would again suggest that SPNs released from the μMESH are more effective than the same nanoparticles administered either systemically (SPNs) or locally (L-SPNs). Also, it is confirmed that DIDL potentiates the cytotoxic activity of DTXL. Notably, the CTRL groups *i.v.* DTXL

and *i.v.* SPNs returned OSs very close to the clinical gold standard (*i.v.* TMZ). Furthermore, the μMESH CTRL groups, namely empty μMESH, DIDL-μMESH and DTXL-μMESH, presented much lower OS as compared with the μMESH. As such, these five therapeutic groups were not further considered.

Fig. 5 | Preclinical therapeutic efficacy of the μ MESH. **a**, Schematic representation of the tumour location for the orthotopic glioblastoma models. **b**, Experimental timeline showing tumour cell inoculation on day 0, treatment initiation on day 15 for U-87 MG Luc⁺ cells (day 53 for patient-derived hCSCs), whole-animal bioluminescence imaging to monitor tumour growth and the final end point (250 d after treatment initiation). **c**, Representative bioluminescence images on day 30 (left) and survival curves (right) of mice subjected to nine different treatments for the no tumour removal model. Note that only the μ MESH group has one mouse still alive at the end of the study (250 d after treatment). Curves are different according to the two-sided log-rank test ($P=0.000041$). **d**, Representative bioluminescence images on day 30 (left) and survival curve (right) of mice subjected to four different treatments for the tumour removal model. Note that the μ MESH group has 90% of mice still alive at the end of the study (250 d after treatment). Curves are different according to the two-sided log-rank test ($P=0.00003$). **e**, Representative bioluminescence images on day 200 (left) and survival curve (right) of mice for the hCSC patient-derived tumour model. Remarkably, all the mice treated with the μ MESH are alive until the end of the experiment, while the whole CTRL group died within 234 d (OS = 154.5 d). (** $P=0.0067$ for two-sided log-rank test.) **f**, Histological analysis of the brain tissue showing the μ MESH on day 30 in a no tumour removal model. The μ MESH (red arrows) is firmly attached to the tumour surface.

The bioluminescence and survival data for the tumour removal model are presented in Fig. 5d (Supplementary Figs. 33–35) for U-87 MG and in Fig. 5e (Supplementary Figs. 36 and 37) for hCSCs. As expected, a marked drop in radiance is observed upon tumour removal, which is then followed by a progressive growth in signal. This clearly documents the existence of post-resection margins and their post-surgery aggressive proliferation (Supplementary Figs. 34e and 37b). Note that the median OS for the CTRL group (no treatment) in the tumour removal model was slightly higher than that for the no tumour removal model (19 versus 14 d— $P=0.027$) (Supplementary Fig. 38).

For the U-87 MG cells, the therapeutic efficacy of the locally deposited μ MESH was directly compared against three CTRL groups—i.v. TMZ, locally administered SPNs (L-SPNs) and the untreated mouse. The μ MESH and L-SPNs were deposited within the resected cavity. The systemic administration of TMZ did not alter the overall median survival (OS 12 d), although one mouse in the group was still alive on day 68 after treatment. Only the μ MESH induced a 250 d survival in 90% of the treated mice. The L-SPNs returned an OS of 36 d (Fig. 5d). A typical histological image taken at 15 d after therapy initiation shows the μ MESH (yellow line) deposited over the growing tumour mass region, establishing an intimate contact with the proliferating tumour cells (Fig. 5f and Supplementary Fig. 39), while inducing a remarkable reduction in tumour mass.

The proneural Luc⁺ hCSCs (L0605) were selected for their characteristic infiltrative nature⁶⁰ and used in a tumour removal model. hCSC tumours showed a much slower growth rate, so tumour removal and treatment started on day 53 rather than 15 (Supplementary Figs. 36 and 37). In this model, the μ MESH eradicated disease recurrence. Specifically, on day 300, all mice treated with the μ MESH presented virtually no bioluminescence signal and were all alive, while 75% of the CTRL mice had succumbed already by day 175 (Fig. 5e and Supplementary Figs. 36 and 37).

In general, the two locally administered treatments, namely L-SPNs and μ MESH, were more effective than all the others. This is not surprising given the presence of the BBB. Notably, in all the experiments, the amounts of DTXL delivered through the μ MESH and L-SPNs were much lower than those provided with the systemic treatments. In fact, only 15 μ g of DTXL was administered once via the μ MESH and L-SPNs, whereas 60 μ g of DTXL was systemically provided for each of the ten single injections. Also, local treatments would reduce the systemic toxicity associated with chemotherapy (Supplementary Fig. 40).

Conclusion

Leveraging the accurate dimensional control offered by nano/micro-fabrication techniques, a hierarchical drug depot (μ MESH) has been engineered to deliver the combination of DTXL-loaded nanomedicines and DICL to malignant gliomas. The modular structure of the μ MESH allows the loading of a broad variety of therapeutic molecules and nanomedicines, potentially including RNA and

immunotherapeutic agents. Furthermore, the absolute amounts of each therapeutic agent can be finely and independently tuned during the fabrication process, thus supporting patient-specific dosing and interventions.

In orthotopic models of glioblastoma, the μ MESH abrogates disease recurrence following resection and extends survival when applied to non-resected tumours. One single μ MESH application is more effective than multiple i.v. administrations of TMZ as well as the one-time intracranial administration of DTXL/DICL-loaded nanoparticles. At 250 d after tumour resection, a single μ MESH application promotes an 80% and 100% survival rate in U-87 MG and hCSC tumours, respectively.

The superior performance of the μ MESH compared with more conventional treatments, such as the systemic administration of TMZ or the intracranial injection of nanomedicines, rests on its ability to conform and interact with complex surfaces, realize a highly localized drug depot and facilitate the deep tissue penetration of the loaded nanomedicines. These features all together represent an ideal combination to improve the prognosis of the most aggressive brain tumour using a battery of combination therapies.

Online content

Any methods, additional references, Nature Research reporting summaries, source data, extended data, supplementary information, acknowledgements, peer review information; details of author contributions and competing interests; and statements of data and code availability are available at <https://doi.org/10.1038/s41565-021-00879-3>.

Received: 11 June 2020; Accepted: 17 February 2021;
Published online: 01 April 2021

References

- Delgado-Lopez, P. D. & Corrales-Garcia, E. M. Survival in glioblastoma: a review on the impact of treatment modalities. *Clin. Transl. Oncol.* **18**, 1062–1071 (2016).
- Omuro, A. & DeAngelis, L. M. Glioblastoma and other malignant gliomas: a clinical review. *JAMA* **310**, 1842–1850 (2013).
- Stupp, R. et al. Maintenance therapy with tumor-treating fields plus temozolomide vs temozolomide alone for glioblastoma: a randomized clinical trial. *JAMA* **314**, 2535–2543 (2015).
- Delgado-Martin, B. & Medina, M. A. Advances in the knowledge of the molecular biology of glioblastoma and its impact in patient diagnosis, stratification, and treatment. *Adv. Sci.* **7**, 1902971 (2020).
- Jackson, C. M., Choi, J. & Lim, M. Mechanisms of immunotherapy resistance: lessons from glioblastoma. *Nat. Immunol.* **20**, 1100–1109 (2019).
- Stupp, R. et al. Radiotherapy plus concomitant and adjuvant temozolomide for glioblastoma. *N. Engl. J. Med.* **352**, 987–996 (2005).
- Aldape, K. et al. Challenges to curing primary brain tumours. *Nat. Rev. Clin. Oncol.* **16**, 509–520 (2019).
- Giese, A., Bjerkvig, R., Berens, M. E. & Westphal, M. Cost of migration: invasion of malignant gliomas and implications for treatment. *J. Clin. Oncol.* **21**, 1624–1636 (2003).
- Stummer, W. et al. Fluorescence-guided surgery with 5-aminolevulinic acid for resection of malignant glioma: a randomised controlled multicentre phase III trial. *Lancet Oncol.* **7**, 392–401 (2006).

10. Lemeec, J. M., Clavreul, A. & Menei, P. Intratumoral heterogeneity in glioblastoma: don't forget the peritumoral brain zone. *Neuro-Oncol.* **17**, 1322–1332 (2015).
11. D'Amico, R. S., Englander, Z. K., Canoll, P. & Bruce, J. N. Extent of resection in glioma—a review of the cutting edge. *World Neurosurg.* **103**, 538–549 (2017).
12. Tanaka, S., Louis, D. N., Curry, W. T., Batchelor, T. T. & Dietrich, J. Diagnostic and therapeutic avenues for glioblastoma: no longer a dead end? *Nat. Rev. Clin. Oncol.* **10**, 14–26 (2013).
13. Ballabh, P., Braun, A. & Nedergaard, M. The blood–brain barrier: an overview: structure, regulation, and clinical implications. *Neurobiol. Dis.* **16**, 1–13 (2004).
14. Lesniak, M. S. & Brem, H. Targeted therapy for brain tumours. *Nat. Rev. Drug Discov.* **3**, 499–508 (2004).
15. Arvanitis, C. D., Ferraro, G. B. & Jain, R. K. The blood–brain barrier and blood–tumour barrier in brain tumours and metastases. *Nat. Rev. Cancer* **20**, 26–41 (2020).
16. The Cancer Genome Atlas Research Network Comprehensive genomic characterization defines human glioblastoma genes and core pathways. *Nature* **455**, 1061–1068 (2008).
17. Network, T. C. Corrigendum: Comprehensive genomic characterization defines human glioblastoma genes and core pathways. *Nature* **494**, 506 (2013).
18. Verhaak, R. G. et al. Integrated genomic analysis identifies clinically relevant subtypes of glioblastoma characterized by abnormalities in PDGFRA, IDH1, EGFR, and NF1. *Cancer Cell* **17**, 98–110 (2010).
19. Wang, Q. et al. Tumor evolution of glioma-intrinsic gene expression subtypes associates with immunological changes in the microenvironment. *Cancer Cell* **33**, 152 (2018).
20. Osuka, S. & Van Meir, E. G. Overcoming therapeutic resistance in glioblastoma: the way forward. *J. Clin. Investig.* **127**, 415–426 (2017).
21. Nefel, C. et al. An integrative model of cellular states, plasticity, and genetics for glioblastoma. *Cell* **178**, 835–849 (2019).
22. Chen, J. et al. A restricted cell population propagates glioblastoma growth after chemotherapy. *Nature* **488**, 522–526 (2012).
23. Lee, A. et al. Spherical polymeric nanoconstructs for combined chemotherapeutic and anti-inflammatory therapies. *Nanomedicine* **12**, 2139–2147 (2016).
24. Lam, F. C. et al. Enhanced efficacy of combined temozolomide and bromodomain inhibitor therapy for gliomas using targeted nanoparticles. *Nat. Commun.* **9**, 1991 (2018).
25. Tamborini, M. et al. A combined approach employing chlorotoxin-nanovectors and low dose radiation to reach infiltrating tumor niches in glioblastoma. *ACS Nano* **10**, 2509–2520 (2016).
26. Prados, M. D. et al. Phase II study of erlotinib plus temozolomide during and after radiation therapy in patients with newly diagnosed glioblastoma multiforme or gliosarcoma. *J. Clin. Oncol.* **27**, 579–584 (2009).
27. Samal, J., Rebelo, A. L. & Pandit, A. A window into the brain: tools to assess pre-clinical efficacy of biomaterials-based therapies on central nervous system disorders. *Adv. Drug Deliv. Rev.* **148**, 68–145 (2019).
28. Randall, E. C. et al. Integrated mapping of pharmacokinetics and pharmacodynamics in a patient-derived xenograft model of glioblastoma. *Nat. Commun.* **9**, 4904 (2018).
29. Foley, C. P. et al. Intra-arterial delivery of AAV vectors to the mouse brain after mannitol mediated blood brain barrier disruption. *J. Control. Release* **196**, 71–78 (2014).
30. Zou, Y. et al. Effective and targeted human orthotopic glioblastoma xenograft therapy via a multifunctional biomimetic nanomedicine. *Adv. Mater.* **30**, e1803717 (2018).
31. Timbie, K. F., Mead, B. P. & Price, R. J. Drug and gene delivery across the blood–brain barrier with focused ultrasound. *J. Control. Release* **219**, 61–75 (2015).
32. Aryal, M., Arvanitis, C. D., Alexander, P. M. & McDaniel, N. Ultrasound-mediated blood–brain barrier disruption for targeted drug delivery in the central nervous system. *Adv. Drug Deliv. Rev.* **72**, 94–109 (2014).
33. May, J. N. et al. Multimodal and multiscale optical imaging of nanomedicine delivery across the blood–brain barrier upon sonopermeation. *Theranostics* **10**, 1948–1959 (2020).
34. Johnsen, K. B. et al. Modulating the antibody density changes the uptake and transport at the blood–brain barrier of both transferrin receptor-targeted gold nanoparticles and liposomal cargo. *J. Control. Release* **295**, 237–249 (2019).
35. Lajoie, J. M. & Shusta, E. V. Targeting receptor-mediated transport for delivery of biologics across the blood–brain barrier. *Annu. Rev. Pharmacol. Toxicol.* **55**, 613–631 (2015).
36. Bu, L. L. et al. Advances in drug delivery for post-surgical cancer treatment. *Biomaterials* **219**, 119182 (2019).
37. Vogelbaum, M. A. & Aghi, M. K. Convection-enhanced delivery for the treatment of glioblastoma. *Neuro-Oncol.* **17**, ii3–ii8 (2015).
38. Brem, H. et al. Placebo-controlled trial of safety and efficacy of intraoperative controlled delivery by biodegradable polymers of chemotherapy for recurrent gliomas. *Lancet* **345**, 1008–1012 (1995).
39. Bota, D. A., Desjardins, A., Quinn, J. A., Affronti, M. L. & Friedman, H. S. Interstitial chemotherapy with biodegradable BCNU (Gliadel) wafers in the treatment of malignant gliomas. *Ther. Clin. Risk Manag.* **3**, 707–715 (2007).
40. Shapira-Furman, T. et al. Biodegradable wafers releasing temozolomide and carmustine for the treatment of brain cancer. *J. Control. Release* **295**, 93–101 (2019).
41. Song, E. et al. Surface chemistry governs cellular tropism of nanoparticles in the brain. *Nat. Commun.* **8**, 15322 (2017).
42. Jahangiri, A. et al. Convection-enhanced delivery in glioblastoma: a review of preclinical and clinical studies. *J. Neurosurg.* **126**, 191–200 (2017).
43. Conde, J., Oliva, N., Zhang, Y. & Artzi, N. Local triple-combination therapy results in tumour regression and prevents recurrence in a colon cancer model. *Nat. Mater.* **15**, 1128–1138 (2016).
44. Talebian, S. et al. Biopolymers for antitumor implantable drug delivery systems: recent advances and future outlook. *Adv. Mater.* **30**, e1706665 (2018).
45. Jain, A. et al. Guiding intracortical brain tumour cells to an extracortical cytotoxic hydrogel using aligned polymeric nanofibres. *Nat. Mater.* **13**, 308–316 (2014).
46. Hosseinzadeh, R. et al. A drug-eluting 3D-printed mesh (GlioMesh) for management of glioblastoma. *Adv. Ther.* **2**, 1900113 (2019).
47. Han, D. et al. Multi-layered core–sheath fiber membranes for controlled drug release in the local treatment of brain tumor. *Sci. Rep.* **9**, 17936 (2019).
48. Ramachandran, R. et al. Theranostic 3-dimensional nano brain-implant for prolonged and localized treatment of recurrent glioma. *Sci. Rep.* **7**, 43271 (2017).
49. Wang, C. et al. In situ formed reactive oxygen species-responsive scaffold with gemcitabine and checkpoint inhibitor for combination therapy. *Sci. Transl. Med.* **10**, eaan3682 (2018).
50. Wang, T. et al. A cancer vaccine-mediated postoperative immunotherapy for recurrent and metastatic tumors. *Nat. Commun.* **9**, 1532 (2018).
51. Lee, J. et al. Flexible, sticky, and biodegradable wireless device for drug delivery to brain tumors. *Nat. Commun.* **10**, 5205 (2019).
52. Theruvath, J. et al. Locoregionally administered B7-H3-targeted CAR T cells for treatment of atypical teratoid/rhabdoid tumors. *Nat. Med.* **26**, 712–719 (2020).
53. Donovan, L. K. et al. Locoregional delivery of CAR T cells to the cerebrospinal fluid for treatment of metastatic medulloblastoma and ependymoma. *Nat. Med.* **26**, 720–731 (2020).
54. Sahoo, S. K., Panyam, J., Prabha, S. & Labhasetwar, V. Residual polyvinyl alcohol associated with poly (D,L-lactide-co-glycolide) nanoparticles affects their physical properties and cellular uptake. *J. Control. Release* **82**, 105–114 (2002).
55. Zweers, M. L., Engbers, G. H., Grijpma, D. W. & Feijen, J. In vitro degradation of nanoparticles prepared from polymers based on DL-lactide, glycolide and poly(ethylene oxide). *J. Control. Release* **100**, 347–356 (2004).
56. Skog, J. et al. Glioblastoma microvesicles transport RNA and proteins that promote tumour growth and provide diagnostic biomarkers. *Nat. Cell Biol.* **10**, 1470–1476 (2008).
57. Dancy, J. G. et al. Non-specific binding and steric hindrance thresholds for penetration of particulate drug carriers within tumor tissue. *J. Control. Release* **238**, 139–148 (2016).
58. Kalb, E. & Engel, J. Binding and calcium-induced aggregation of laminin onto lipid bilayers. *J. Biol. Chem.* **266**, 19047–19052 (1991).
59. Wong, C. et al. Multistage nanoparticle delivery system for deep penetration into tumor tissue. *Proc. Natl Acad. Sci. USA* **108**, 2426–2431 (2011).
60. Narayanan, A. et al. The proneural gene ASCL1 governs the transcriptional subgroup affiliation in glioblastoma stem cells by directly repressing the mesenchymal gene NDRG1. *Cell Death Differ.* **26**, 1813–1831 (2019).

Publisher's note Springer Nature remains neutral with regard to jurisdictional claims in published maps and institutional affiliations.

© The Author(s), under exclusive licence to Springer Nature Limited 2021

Methods

Fabrication of the μ MESH. A top-down approach was developed to fabricate the μ MESH. First, a master silicon template, reproducing the specific μ MESH geometrical pattern, was realized. The pattern consisted of an ordered series of pillars, with a $20\ \mu\text{m}^2$ base length and a $5\ \mu\text{m}$ height, separated by a $3\ \mu\text{m}$ gap. This silicon master was realized using the direct laser writing technique. Specifically, chrome was deposited by evaporation on top of a silicon wafer and then coated with a photopolymerizable resist (AZ5214E). Polymer crosslinking was realized by exposure to laser light at $405\ \text{nm}$. Following the Bosch process, deep reactive ion etching was used to dig into the silicon wafer to the required depth. Finally, chrome and resist were removed from the silicon wafer. The resulting silicon master template was replicated in a PDMS template by casting PDMS (elastomer:curing agent ratio equal to 10:1) onto it. From this negative template, a PVA template was obtained by simply adding the PVA solution on top of the PDMS and drying it at 60°C for 3 h. The final PVA layer presented the same geometry of the pillars as the silicon master. Within the PVA solution, any hydrophilic molecules or nanoparticle could be readily dispersed.

For the realization of the μ MESH, a polymeric paste was uniformly deposited over the PVA layer, already including SPNs. This returned a continuous microscopic mesh structure with $3\ \mu\text{m}$ strands separated by holes of $20 \times 20\ \mu\text{m}^2$. The polymeric paste was composed of PLGA. Any hydrophobic molecule could be readily added to the PLGA paste. Specifically, in the context of this work, either CURC or DICL was added to the PLGA paste. For the μ MESH, $5\ \text{mg}$ of PLGA mixed with $500\ \mu\text{g}$ of CURC or different amounts of DICL, namely 50 , 500 and $1,000\ \mu\text{g}$, were used per template. For all the experiments, the μ MESH size was $5 \times 5\ \text{mm}^2$, derived by precisely cutting the original $3 \times 2.5\ \text{cm}^2$ template with a surgical scalpel.

Loading and release of DICL in the μ MESH. The amount of DICL dispersed within the μ MESH PLGA strands was calculated for three different feeding amounts, namely 50 , 500 and $1,000\ \mu\text{g}$ ($n > 10$ for each condition), via high-performance liquid chromatography (HPLC) analysis (DICL absorbance at $280\ \text{nm}$). To analyse the DICL release, the μ MESH was placed in tubes ($n = 10$) filled with $1\ \text{ml}$ of PBS, and kept at 37°C . This volume was selected as it is comparable to the volume to which the μ MESH would be exposed *in vivo* upon intracranial implantation. At each time point, tubes were centrifuged at $15,000\ g$ for $5\ \text{min}$ to separate the supernatant with the released DICL from the μ MESH. Then, the pelleted μ MESH, carrying the residual amount of DICL, was dissolved in acetonitrile:water (1:1). The resulting unreleased amounts of DICL were analysed via HPLC. Release data were presented in the form of cumulative percentage release (Supplementary Fig. 9b) as described for the DTXL-SPNs.

Aqueous dissolution of the PVA layer. An SEM was used to image the μ MESH at different time points, namely before contact with an aqueous solution, after $30\ \text{min}$ and after overnight incubation. μ MESHes were placed on a silicon substrate, sputter-coated with $15\ \text{nm}$ of gold and then imaged at $15\ \text{keV}$ using an analytical low-vacuum SEM (JSM-6490, JEOL).

Release of molecules and nanoparticles from the PVA layer. Either free RhB molecules or RhB-SPNs were included in the PVA solution to eventually obtain the corresponding μ MESH. This was also loaded with the green fluorescent CURC to enhance the contrast between the PLGA mesh (green) and the PVA layer (red). The resulting μ MESH was placed on the bottom of a Petri dish. Then, it was imaged over time via epifluorescent microscopy, while PBS was continuously added to dissolve the PVA layer, from which particles were progressively released. At different time points, ranging between $15\ \text{s}$ and $10\ \text{min}$, fluorescence intensity profiles were recorded along 18 parallel lines, running orthogonally to the μ MESH edge deep into the PBS solution up to $500\ \mu\text{m}$ (Supplementary Figs. 1 and 2). For each time point, the amounts of released free RhB or RhB-SPNs were determined by normalizing the measured fluorescent intensities along the 18 parallel lines by the averaged fluorescent intensities detected at the μ MESH edge ($20\ \mu\text{m}$ width).

Loading and embedding efficiency of nanoparticles in the PVA layer. Different volumes of DTXL-SPNs, namely 1 , 5 , 50 , 200 and $500\ \mu\text{l}$, at a fixed concentration of $1\ \text{mM}$, were added to the PVA solution before realizing the PVA layer. Using HPLC and following the protocols described above for the release of nanoparticles from the PVA layer and drug loading into SPNs, the loading and embedding efficiency of DTXL was determined for all the tested PVA configurations ($n = 10$). The embedding efficiency was calculated as the percentage ratio between the final DTXL amount in the entire μ MESH template (that is, 30 single μ MESHes) and the DTXL input in the SPN-enriched PVA solution used for μ MESH fabrication.

Interaction of tumour spheroids with the μ MESH. FLAT was fabricated by spreading the PLGA polymeric paste over a flat PVA layer. μ MESH and FLAT were loaded with different amounts of DTXL, namely 5 , 25 , 50 and $75\ \mu\text{g}$, following the same procedures as described above for the μ MESH. DTXL loading was assessed via HPLC analysis upon dissolving a $5 \times 5\ \text{mm}^2$ piece, derived from either the μ MESH or FLAT, in an acetonitrile:water (1:1) solution. For the release study, the μ MESH or FLAT were placed in tubes with $1\ \text{ml}$ of PBS and kept at 37°C . At the

desired time points, the PBS was removed and substituted with fresh PBS. The collected PBS was mixed with acetonitrile:water (1:1) and analysed using HPLC.

For the therapeutic experiments, μ MESH or FLAT were deposited at the bottom of a PDMS-coated Petri dish. Subsequently, tumour spheroids of U-87 MG GFP⁺ cells ($n = 4$ per condition) were positioned on top of the μ MESH or FLAT surface, and after $2\ \text{h}$ fresh medium was added. After $24\ \text{h}$, the samples resulting from the interaction of the tumour spheroids with either the μ MESH or FLAT were prepared for confocal microscopy, SEM and TEM imaging analyses. In the first case, the μ MESH or FLAT was also previously loaded with RhB to better distinguish it from the spheroid. Samples were gently washed with PBS, fixed with a 4% paraformaldehyde solution and washed again three times. Finally, samples were imaged using confocal microscopy (Plan Apo $\times 20$, Nikon A1). For the SEM analyses, the samples were fixed with glutaraldehyde 2% in a sodium cacodylate buffer, $0.1\ \text{M}$ at pH 7.4 , and then post-fixed with 1% osmium tetroxide solution, dehydrated with an alcohol series at 4°C and infiltrated with hexamethyldisilazane. After overnight drying, samples were sputter-coated with a thin ($10\ \text{nm}$) layer of gold. Imaging was performed with an analytical low-vacuum SEM (JSM-6490, JEOL) at $15\ \text{kV}$. To prepare the samples for TEM imaging, spheroids were fixed with glutaraldehyde 2% in a sodium cacodylate buffer, $0.1\ \text{M}$ at pH 7.4 , post-fixed with 1% osmium tetroxide solution, dehydrated with an alcohol series at 4°C and subsequently infiltrated with Lowicryl resin under ultraviolet light ($360\ \text{nm}$). Finally, the region of the spheroids in contact with the FLAT or the μ MESH was cut into $70\ \text{nm}$ -thick slices and imaged using a TEM ($100\ \text{kV}$, JEOL JEM-10119).

For the cytotoxic efficacy study, the μ MESH or FLAT were prepared by dispersing $0.5\ \mu\text{g}$ of DTXL in the polymeric paste to obtain a $0.1\ \mu\text{M}$ drug concentration in the well. Spheroids were added to the dish as described above for the imaging experiments. The area of the spheroids was monitored over time, relying on the green fluorescence signal provided by the U-87 MG GFP⁺ cells.

Cytotoxicity of the μ MESH on tumour cell spheroids. 500 U-87 MG GFP⁺ cells were seeded in a Gravity TRAP ULA plate (inSphero) following the manufacturer's protocol. After $1\ \text{d}$, spheroids were transferred to a 48 -well plate, whose bottom was covered with PDMS to avoid spheroid adhesion and limit the diffusion of medium and drugs within its impermeable matrix. Different initial numbers of cells, namely 200 , 500 , $1,000$ and $2,500$, were considered to form spheroids of different sizes. For the chosen number of initial U-87 MG GFP⁺ cells (500), spheroids grew moderately fast, and at $10\ \text{nM}$ DTXL the spheroid diameter halved within $72\ \text{h}$, similarly to the cell monolayer (Supplementary Fig. 12). Spheroids were exposed to different therapeutic groups for a week ($n = 4$ per condition): free DTXL, free DICL, free DTXL/DICL combination at $1:5$ ratio w/w, DTXL-loaded SPNs from the PVA template (μ SPNs), the μ MESH loaded with DICL and carrying the DTXL-SPNs, and the empty μ MESH. For DTXL-related treatment, the concentrations used were 1 , 10 , 50 , 100 and $1,000\ \text{nM}$. The DICL concentration was five times higher than that of DTXL when used in combination²³. In one study, the amount of DICL was kept fixed at $15\ \mu\text{g}$, mimicking the preferred loading condition of DICL into the μ MESH (that is, the case with $1\ \text{mg}$ of DICL for input). Also for the μ MESH, the amount of DICL was fixed to be $15\ \mu\text{g}$, with a final concentration of around $50\ \mu\text{M}$. Over 1 week, the area of the spheroids was monitored, relying on the U-87 MG GFP⁺ green fluorescence signal. At each time point, the equatorial surface was considered using the software ImageJ (NIH) to extrapolate the area. The growth rate was estimated as the percentage increase of the spheroid equatorial radius on a particular day compared with the size on day 0.

Finally, a ReadyProbes cell viability imaging kit (Molecular Probes) was used to quantify the proportions of live and dead cells within the spheroid. At the end of the treatment, the dye propidium iodide, which recognizes dead cells, was added to each well, and after an incubation time of $20\ \text{min}$ the spheroids were imaged. The fluorescence intensity was then used to calculate the percentage increase in dead cells compared with CTRL spheroids. To this end, after background subtraction, two extreme conditions were defined, namely 0 and 100% cell viability. The latter was the average fluorescent value associated with the untreated spheroids (CTRL), whilst the former corresponded to the highest fluorescence intensity in each treatment condition. From this analysis, an IC_{50} value was derived for each treatment type and concentration.

Depth of penetration of nanoparticles in Matrigel. Matrigel was used as a model matrix to mimic a three-dimensional extracellular environment. A solution of $10\ \text{mg}\ \text{ml}^{-1}$ of Matrigel was poured into an eight-well microscopy glass slide and left to polymerize at 37°C . Then RhB-SPNs and RhB- μ SPNs (released from a PVA layer) were dispersed into cell culture medium and deposited on top of the Matrigel. Then, using confocal microscopy, the nanoparticle dynamics was followed over time, taking still images at 4 , 12 , 24 and $36\ \text{h}$ ($n = 6$ for each group). The top and bottom of the Matrigel were properly identified along the z axis. The fluorescent profile associated with the nanoparticles was quantified along the z axis using ImageJ. The fluorescence intensity at time 0 was used as the baseline so that fluorescent intensities at later time points were expressed as a percentage variation of the time 0 value, along the z axis.

Depth of penetration of nanoparticles in tumour spheroids. Preformed U-87 MG GFP⁺ spheroids were placed in contact for $2\ \text{h}$ with a U-87 MG monolayer to

firmly anchor them at the bottom of a glass slide. Then, spheroids were incubated with SPNs and μ SPNs ($n=3$ for each condition). However, in this case, both nanoparticles were tagged with Cy5 and loaded with 10 nm AuNPs. By using a fluorescent reporter (Cy5) and an electron dense agent (AuNPs), CLEM imaging was adopted to locate the nanoparticles deep in the spheroids. Nanoparticles were incubated with the spheroids for 24 h. Then, spheroids were fixed with 4% paraformaldehyde + 0.1% glutaraldehyde in a sodium cacodylate buffer, 0.1 M at pH 7.4, post-fixed with 1% osmium tetroxide solution, dehydrated with an alcohol series at 4°C and subsequently infiltrated with Lowicryl resin under ultraviolet light (360 nm). This resin could infiltrate and polymerize within the spheroids without damaging its structure or the nanoparticles. Finally, resin blocks were cut every 10 μ m from the slide anchorage point of the spheroids in two 70-nm-thick slices. One of these was placed on a glass slide for confocal microscopy imaging, while the other was placed onto formvar-coated finder grids for CLEM imaging. To evaluate the penetration in the spheroids, confocal microscopy images were individually analysed, drawing circular concentric ROIs of different sizes from the centre of the spheroids to the outer surface (Fig. 4d). The mean fluorescence of each ROI was normalized to the mean fluorescence of the more external region, fixed as a reference to 100%. Data were presented as percentage of fluorescence intensity to account for the fact that slides were exposed to light for different times during the cutting of the resin blocks. Finally, data from each slice were collected into three groups, representing different regions of the spheroids from the bottom to the equatorial plane, namely the 10–50 μ m region, the 60–100 μ m region and the 110–150 μ m region. For CLEM, spheroid slices were placed onto finder grids to facilitate the identification of ROIs by proper markers. The slices were first imaged using the confocal microscope and those presenting fluorescent signals were also analysed with the TEM (100 kV, JEOL JEM-10119).

Depth of penetration of nanoparticles in brains of tumour-bearing mice.

After establishing an orthotopic intracranial GBM model, on the first day of therapy, Cy5-SPNs and an SPN-loaded μ MESH were deposited on top of the brain surface. After 8 d, mice were killed and their brains were collected, fixed in 4% paraformaldehyde and frozen sectioned using a microtome–cryostat with a 10 μ m slice. The sections were then placed on HistoBond microscope slides (Marienfeld) and stained with 4,6-diamidino-2-phenylindole to facilitate the identification of the ROI. Brain slices were imaged using a confocal microscope (Nikon) in a 2.5-mm-long and 2.5-mm-deep region, matching the site of application. This region was analysed, measuring the average fluorescence intensity profile along the z axis of 12 parallel distinct rectangular areas with dimensions 200 μ m wide and 2.5 mm deep. For each slice, data were normalized to percentages, defining the maximum value of fluorescent intensity in the whole slice as 100%, and then grouped and averaged every seven z -stack positions (approximately 10 μ m).

Orthotopic brain tumour models. For the orthotopic intracranial GBM tumour model, 5–6-week-old female athymic nude mice were stereotactically inoculated with U-87 MG Luc⁺ cells (Charles River). Animals were grouped in ventilated cages and able to freely access food and water. They were maintained under controlled conditions: temperature ($21 \pm 2^\circ\text{C}$), humidity ($50 \pm 10\%$) and light (12 h of light and 12 h of dark). All animal experiments were performed according to the guidelines established by the European Communities Council Directive (2010/63/EU of 22 September 2010) and approved by the National Council on Animal Care of the Italian Ministry of Health. All efforts were made to minimize animal suffering and use the smallest possible number of animals required to produce statistically relevant results, according to the ‘3Rs’ (replacement, reduction and refinement) concept. Before cell injection, animals were anaesthetized with a mixture of ketamine (100 mg kg⁻¹) and xylazine (10 mg kg⁻¹), administered via a single intraperitoneal injection. For tumour development, 5×10^5 U-87 MG Luc⁺ cells were resuspended in 3 μ l cold PBS and injected into the right hemisphere of the mouse brain (1.5 mm posterior to the bregma, 1.4 mm lateral to the midline and 1 mm or 0.75 mm depth from the skull, on the basis of the model). Cells were injected at a speed of 0.3 μ l min⁻¹ using a 10 μ l sterile Hamilton syringe fitted with a 26-gauge needle attached to a stereotaxic frame. Wounds were closed with sterile wound clips, and animals were carefully monitored until they had recovered from anaesthesia. Tumour growth was followed using an IVIS Spectrum (Perkin Elmer) every 2 d, and analysed with Living Image 4.5.5 (Perkin Elmer).

For the model without tumour removal, when tumours reached an average radiance of about 1×10^6 , mice were randomly divided into different treatment groups: saline (CTRL, $n=9$), i.v. TMZ (3 mg kg⁻¹ every other day, $n=9$), i.v. DTXL (3 mg kg⁻¹ every other day, $n=9$), DTXL/DICL-SPNs (systemic SPNs, 3 mg kg⁻¹ every other day, $n=9$), empty μ MESH ($n=5$), DICL- μ MESH ($n=5$), DTXL- μ MESH ($n=7$), locally administered DTXL/DICL-SPNs (L-SPNs, $n=7$) and μ MESH ($n=10$). For L-SPNs and μ MESH, 0.75 mg ml⁻¹ (that is, 15 μ g) of DTXL was administered. For the case of DICL- μ MESH, the same amount of DICL as used for the μ MESH mice (that is, 0.75 mg kg⁻¹) was used.

For the tumour removal animal model, before starting the treatment, a larger hole of about 3 mm was realized at the same stereotactic coordinates by using a trephine—2.7 mm diameter. The portion of the tumour closer to the surface was resected using a scalpel. Then, the skull was sealed using a drop of silicon elastomer and mice were divided into four treatment groups: saline (CTRL, $n=9$),

i.v. TMZ (3 mg kg⁻¹ every other day, $n=7$), L-SPNs ($n=6$) and μ MESH ($n=8$). In this model too, L-SPNs and μ MESH were loaded with 0.75 mg ml⁻¹ of DTXL.

Regarding the patient-derived xenograft model, tumour cells were stably transfected to be Luc⁺. Tumour growth was monitored using the IVIS Spectrum system as for the U-87 MG cases. The only difference was that the primary human cells grew as neurospheres in NeuroCult NS-A (STEMCELL Technologies), thus before intracranial injection they were dissociated by gentle repetitive pipetting, avoiding any cell damage. Surgical operation, treatment and follow-up were performed as in the recurrence model. For this model, mice were divided into two groups, namely saline (CTRL, $n=4$) and μ MESH (0.75 mg ml⁻¹ DTXL, $n=4$). In all the different orthotopic tumour models, whole-animal imaging with the IVIS Spectrum was performed the day after the surgery to assess tumour resection, avoiding any additional stress to the animals. The average radiance was assessed using the Living Image 4.5.5 software (Perkin Elmer), drawing a circular ROI (2 cm in diameter), kept constant for all the mice at all time points analysed. All mice were euthanized at the onset of neurological or systemic deficits. Survival curves were plotted using the Kaplan–Meier method. The two-sided log-rank test was used to test the statistically significant difference in survival curves.

Statistical analyses and reproducibility. When comparing two groups, an F test was used to check for the absence of statistical significantly different variances, followed by the two-tailed t -test. Multiple comparisons (that is, three or more groups to compare in the same experiment) were performed using the Brown–Forsythe test for the equality of variance among the groups, followed by a one-way analysis of variance test. The Tukey post hoc test was used to discriminate differences in two-pair comparisons. All the tests and the graphs were performed and realized using GraphPad Prism. Differences were considered statistically significant when returning a P value lower than 0.05. All the experiments were performed at least three times independently, and results were reproducible.

Reporting Summary. Further information on research design is available in the Nature Research Reporting Summary linked to this article.

Data availability

The data that support the plots within this paper and other findings of this study are available from the corresponding author upon reasonable request.

Acknowledgements

This project was partially supported by the European Research Council under the European Union's Seventh Framework Programme (FP7/2007–2013)/ERC grant agreement 616695–POTENT (P.D.), and by the European Union's Horizon 2020 Research and Innovation Programme under the Marie Skłodowska-Curie grant agreement 754490–MINDED (P.D.). We thank the laboratory of D. De Pietri Tonelli for providing the U-87 MG GFP⁺ cells. We thank the Clean Room Facility in IIT and M. Francardi, P.D. and G.A.G. are grateful to Professor Sanjiv Sam Gambhir of Stanford University for catalysing and supporting the collaboration between their laboratories. We dedicate this work to the memory and legacy of Professor Sanjiv Sam Gambhir, who passed away on 18 June 2020.

Author contributions

D.D.M. and P.D. conceived the idea and designed the experiments. D.D.M. realized all the different platforms used, performed all the in vitro experiments, acquired optical and electron microscopy images, analysed all the data and performed statistical analyses. A.L.P. performed all the in vivo experiments. R.P. conducted the histological analyses and sample preparation. F.M. helped in the realization of the orthotopic tumour models. T.C. prepared samples for CLEM study. F.P. and R.S. helped with the in vivo experiments. A.L.G. and R.G. provided patient-derived GBM cells, transfected the cells with Luc⁺ and helped in developing the tumour model, and A.L.G. helped with cell inoculation. M.F. synthesized lipid-Cy5. R.M. performed cryo-EM analyses. A.A. performed liquid chromatography–mass spectrometry analyses. C.W. and G.A.G. performed time-course penetration experiments with μ SPNs. D.D.M., P.D. and A.L.P. wrote the manuscript. P.D. supervised the whole project.

Competing interests

D.D.M. and P.D. are the coinventors on the pending patent WO2019193524A1—‘An implantable device for localized drug delivery, uses thereof and a manufacturing method thereof’ filed by the Fondazione Istituto Italiano di Tecnologia. The remaining authors declare no competing interests.

Additional information

Supplementary information The online version contains supplementary material available at <https://doi.org/10.1038/s41565-021-00879-3>.

Correspondence and requests for materials should be addressed to P.D.

Peer review information *Nature Nanotechnology* thanks Manish Aghi, Ravi Bellamkonda and Abhay Pandit for their contribution to the peer review of this work.

Reprints and permissions information is available at www.nature.com/reprints.

Reporting Summary

Nature Research wishes to improve the reproducibility of the work that we publish. This form provides structure for consistency and transparency in reporting. For further information on Nature Research policies, see our [Editorial Policies](#) and the [Editorial Policy Checklist](#).

Statistics

For all statistical analyses, confirm that the following items are present in the figure legend, table legend, main text, or Methods section.

n/a Confirmed

- | | | |
|-------------------------------------|-------------------------------------|--|
| <input type="checkbox"/> | <input checked="" type="checkbox"/> | The exact sample size (n) for each experimental group/condition, given as a discrete number and unit of measurement |
| <input type="checkbox"/> | <input checked="" type="checkbox"/> | A statement on whether measurements were taken from distinct samples or whether the same sample was measured repeatedly |
| <input type="checkbox"/> | <input checked="" type="checkbox"/> | The statistical test(s) used AND whether they are one- or two-sided
<i>Only common tests should be described solely by name; describe more complex techniques in the Methods section.</i> |
| <input type="checkbox"/> | <input checked="" type="checkbox"/> | A description of all covariates tested |
| <input type="checkbox"/> | <input checked="" type="checkbox"/> | A description of any assumptions or corrections, such as tests of normality and adjustment for multiple comparisons |
| <input type="checkbox"/> | <input checked="" type="checkbox"/> | A full description of the statistical parameters including central tendency (e.g. means) or other basic estimates (e.g. regression coefficient) AND variation (e.g. standard deviation) or associated estimates of uncertainty (e.g. confidence intervals) |
| <input type="checkbox"/> | <input checked="" type="checkbox"/> | For null hypothesis testing, the test statistic (e.g. F , t , r) with confidence intervals, effect sizes, degrees of freedom and P value noted
<i>Give P values as exact values whenever suitable.</i> |
| <input checked="" type="checkbox"/> | <input type="checkbox"/> | For Bayesian analysis, information on the choice of priors and Markov chain Monte Carlo settings |
| <input checked="" type="checkbox"/> | <input type="checkbox"/> | For hierarchical and complex designs, identification of the appropriate level for tests and full reporting of outcomes |
| <input checked="" type="checkbox"/> | <input type="checkbox"/> | Estimates of effect sizes (e.g. Cohen's d , Pearson's r), indicating how they were calculated |

Our web collection on [statistics for biologists](#) contains articles on many of the points above.

Software and code

Policy information about [availability of computer code](#)

Data collection Confocal microscopy images were acquired by NIS-Elements AR 4.5 (Nikon), while Bio-luminescent data were collected by Living Image 4.5.5 (Perkin Elmer).

Data analysis All statistical analyses were performed by Graphpad Prism 8. ImageJ 1.52n was used to analyze fluorescent images. Living Image 4.5.5 (Perkin Elmer) was used to analyze bioluminescent images.

For manuscripts utilizing custom algorithms or software that are central to the research but not yet described in published literature, software must be made available to editors and reviewers. We strongly encourage code deposition in a community repository (e.g. GitHub). See the Nature Research [guidelines for submitting code & software](#) for further information.

Data

Policy information about [availability of data](#)

All manuscripts must include a [data availability statement](#). This statement should provide the following information, where applicable:

- Accession codes, unique identifiers, or web links for publicly available datasets
- A list of figures that have associated raw data
- A description of any restrictions on data availability

The data that support the plots within this paper and other findings of this study are available from the corresponding author upon reasonable request.

Field-specific reporting

Please select the one below that is the best fit for your research. If you are not sure, read the appropriate sections before making your selection.

Life sciences Behavioural & social sciences Ecological, evolutionary & environmental sciences

For a reference copy of the document with all sections, see [nature.com/documents/nr-reporting-summary-flat.pdf](https://www.nature.com/documents/nr-reporting-summary-flat.pdf)

Life sciences study design

All studies must disclose on these points even when the disclosure is negative.

Sample size	No statistical methods were used to predetermine the sample sizes, but the ones employed in this study are consistent with previously published works (e.g., Xu, J., Lv, J., Zhuang, Q. et al. A general strategy towards personalized nanovaccines based on fluoropolymers for postsurgical cancer immunotherapy. Nat. Nanotechnol. 15, 1043–1052 (2020).
Data exclusions	No data were excluded
Replication	All the experiments were performed at least three times independently. The experimental findings were reproducible.
Randomization	All the samples for the in vitro and in vivo experiments were selected randomly.
Blinding	Blinding was not relevant in this study. Indeed, results were quantitative and not qualitative, and, as such, not influenced by human interpretation. Nonetheless, the in vivo studies were partially blinded to group allocation, as therapeutic treatment and data analysis were performed by different scientists.

Reporting for specific materials, systems and methods

We require information from authors about some types of materials, experimental systems and methods used in many studies. Here, indicate whether each material, system or method listed is relevant to your study. If you are not sure if a list item applies to your research, read the appropriate section before selecting a response.

Materials & experimental systems

n/a	Involvement in the study
<input checked="" type="checkbox"/>	<input type="checkbox"/> Antibodies
<input type="checkbox"/>	<input checked="" type="checkbox"/> Eukaryotic cell lines
<input checked="" type="checkbox"/>	<input type="checkbox"/> Palaeontology and archaeology
<input type="checkbox"/>	<input checked="" type="checkbox"/> Animals and other organisms
<input checked="" type="checkbox"/>	<input type="checkbox"/> Human research participants
<input checked="" type="checkbox"/>	<input type="checkbox"/> Clinical data
<input checked="" type="checkbox"/>	<input type="checkbox"/> Dual use research of concern

Methods

n/a	Involvement in the study
<input checked="" type="checkbox"/>	<input type="checkbox"/> ChIP-seq
<input checked="" type="checkbox"/>	<input type="checkbox"/> Flow cytometry
<input checked="" type="checkbox"/>	<input type="checkbox"/> MRI-based neuroimaging

Eukaryotic cell lines

Policy information about [cell lines](#)

Cell line source(s)	U-87 MG cells were obtained from ATCC. U-87 MG GFP+ cells were provided by the laboratory of Dr. Davide De Pietri Tonelli (Italian Institute of Technology, Genova, IT), starting from the ATCC counterpart. U-87 MG Luc+ cells were obtained from Perkin Elmer. The proneural LUC+ hCSC line (L0605) were isolated from a patient with glioblastoma multiforme at the Hospital San Raffaele in Milano by Dr. Alberto Gallotti and Dr. Rossella Galli, and then stably LUC transfected.
Authentication	Cell lines identities were frequently checked for their morphological features but have not been authenticated by the short tandem repeat (STR) profiling.
Mycoplasma contamination	All cell lines were tested for mycoplasma contamination. No mycoplasma contamination was found
Commonly misidentified lines (See ICLAC register)	Despite the fact that U-87 MG still represent a reference in the field, recently the one from ATCC were proved to be different from the original Uppsala University's collection. This was proved by Allen et al. (Science Translational Medicine; 8:354; 354re3), still declaring those cell as a bona fide human glioblastoma cell line of unknown origin.

Animals and other organisms

Policy information about [studies involving animals](#); [ARRIVE guidelines](#) recommended for reporting animal research

Laboratory animals	For the experiments, 5-6 week old female athymic nude mice (Charles River) were used.
Wild animals	The study did not involve wild animals.
Field-collected samples	The study did not involve samples collected from the field.
Ethics oversight	All animal experiments were performed according to the guidelines established by the European Communities Council Directive (Directive 2010/63/EU of 22 September 2010) and approved by the National Council on Animal Care of the Italian Ministry of Health.

Note that full information on the approval of the study protocol must also be provided in the manuscript.